

Simple calculation of a computer-generated hologram for lensless holographic 3D projection using a nonuniform sampled wavefront recording plane

CHENLIANG CHANG,¹ JUN WU,² YIJUN QI,² CAOJIN YUAN,¹ SHOUPING NIE,^{1,*} AND JUN XIA^{2,3}

¹Jiangsu Key Laboratory for Opto-Electronic Technology, School of Physics and Technology, Nanjing Normal University, Nanjing, 210023, China

²Joint International Research Laboratory of Information Display and Visualization, School of Electronic Science and Engineering, Southeast University, Nanjing, 210096, China

³e-mail: xiajun@seu.edu.cn

*Corresponding author: nieshouping@njnu.edu.cn

Received 22 July 2016; revised 31 August 2016; accepted 31 August 2016; posted 1 September 2016 (Doc. ID 272147); published 28 September 2016

In this paper, we present a method for calculation of a computer-generated hologram (CGH) from a 3D object. A virtual wavefront recording plane (WRP) which is close to the 3D object is established. This WRP is nonuniformly sampled according to the depth map of the 3D object. The generation of CGH only involves two nonuniform fast Fourier transform (NUFFT) and two fast Fourier transform (FFT) operations, the whole computational procedure is greatly simplified by diffraction calculation from a 2D planar image instead of 3D object voxels. Numerical simulations and optical experiments are carried out to confirm the feasibility of our proposed method. The CGH calculated with our method is capable to project zoomable 3D objects without lens. © 2016 Optical Society of America

OCIS codes: (090.0090) Holography; (090.2870) Holographic display; (090.1760) Computer holography; (050.1940) Diffraction.

<http://dx.doi.org/10.1364/AO.55.007988>

1. INTRODUCTION

The holographic projection technique which utilizes a computer-generated hologram (CGH) has attracted considerable attention for its high diffraction efficiency, low power consumption, high-contrast, and wide color gamut images [1,2]. The most promising advantage of holographic projection over traditional projection techniques lies in its ability to project images without using lenses. By removing the lenses system and other related bulk mechanical devices, lensless holographic projection shows great potential toward miniaturization and low-cost in laser-based projection devices.

In lensless holographic projection, a computer-generated hologram (CGH) is first calculated from the image we intend to project. Different types of commercial spatial light modulators (SLMs) are employed to load the CGH for projecting image. The CGH can be calculated from the image based on the angular spectrum method [3] or the Fresnel diffraction [4,5], in which the fast Fourier transform (FFT) is used for fast calculation. Furthermore, Shimobaba also proposed a method named *ARSS-Fresnel diffraction* to calculate CGH, which is a scaled Fresnel diffraction calculation that calculates diffraction at different sampling rates on a projected image and

hologram [6]. This type of CGH can realize the zoom function of the projected image without using zoom lenses [7]. However, the above technologies have limitations in terms of their inaccessibility of 3D image reconstruction.

Given that the hologram has potential for reconstructing all the three-dimensional (3D) information of an object in space, we aim to develop holographic 3D projection technique based on the calculation of CGH from a 3D object. Compared with holographic image projection, one serious problem in holographic 3D projection is derived from the huge amount of points of 3D objects, resulting in long calculation time in CGH generation. During the past decades, numerous methods have been proposed to accelerate the calculation of CGH. The point-based method with look-up tables is an effective method in that this method precalculates wavefronts of point light sources [8–10]. However, an inevitable drawback brought with the method is its requirement for a large amount of memory space storing the precalculated wavefront. The layer-based methods [11–13] and the polygon-based methods [14–16] have been proposed based on the idea of converting the diffraction calculation from object points to planes, in which the calculation can be accelerate based on the developed Fresnel

diffraction algorithms between planes. Nevertheless, modeling a 3D object into numerous planes (sometimes more than tens of thousands planes) remains a cumbersome process. Additionally, special software is required, and time consumption is proportional to the numbers of the modeled planes.

One promising and fastest approach for CGH generation, is the wavefront recording plane (WRP) method proposed by Shimobaba [17–19]. In this method, a virtual 2D WRP that is close to the object scene is derived. The CGH is generated by executing diffraction calculation from the WRP to the hologram. The computation burden is dramatically reduced because for each object point only a small zone of diffraction fringe patterns is determined. Nevertheless, the calculation from the object points to the WRP still accounts for a considerable amount of computation time that is proportional to the number of object points. This problem can be further overcome by nonuniformly sampling the object points and warping the WRP proposed by Tsang [20]. However, due to the fact that the hologram is generated by the angular spectrum method from the warped WRP with mapped value, it still remains a challenge to project a 3D object larger than the CGH size.

In this paper, we propose a simple and generalized method for calculating the CGH of a 3D object. A nonuniform sampled WRP is designed and calculated from the object by using the nonuniform sampled fast Fourier transform (NUFFT) algorithm, which allows calculating the WRP in a simple and direct way. NUFFT is an algorithm to calculate the Fourier transform when the sampling pitch in either the spatial domain or the frequency domain is nonuniform [21–23]. Generally, the NUFFT can be categorized into two types: the first type is the calculation from nonuniform sampled points to uniform sampled points (type 1) and the second type (type 2) is versa. A NUFFT-based algorithm has been developed in a variety of directions including diffraction calculation and computer holography. For example, the scaled diffraction calculation method based on NUFFT have been proposed by Shimobaba [24,25] and was used to calculate CGH from a 3D object modeled by polygons [26]. Another method for calculating CGH from multilayered 3D object using NUFFT was also reported [27]. In this paper, we use the Greengard and Lee NUFFT method [23] which is based on the oversampled gridding to calculate the WRP. The CGH is obtained by diffraction calculation from the WRP using ARSS-Fresnel diffraction reported in [6]. The generated CGH can project a 3D object with perceptive depth, zoomable function in a lenless holographic 3D projection system.

2. METHODS

A. Diffraction between Planes with Different Sampling Pitches

To begin with, the diffraction property between two planes with variable sampling rate is discussed. A schematic illustration of diffraction between planes *A* and *B* is presented in Fig. 1(a). Assuming that $A(x_1, y_1)$ and $B(x_2, y_2)$ represent the light field in planes *A* and *B*, respectively. The relations between planes *A* and *B* can be expressed according to the Fresnel diffraction integral as follows:

$$B(x_2, y_2) = \iint A(x_1, y_1) \cdot \exp \left\{ \frac{i\pi}{\lambda z} [(x_2 - x_1)^2 + (y_2 - y_1)^2] \right\} dx_1 dy_1, \quad (1)$$

where λ is the wavelength, and z is the distance between planes *A* and *B*. Now when the light field of plane *A* is stretched, which means the sampling pitch of points is scaled, for example, from (x_1, y_1) to (ax_1, ay_1) . To maintain the value of light field of plane *B*, Eq. (1) should be rewritten to:

$$\begin{aligned} B(ax_2, ay_2) &= \iint A(ax_1, ay_1) \\ &\cdot \exp \left\{ \frac{i\pi}{\lambda a^2 z} [(ax_2 - ax_1)^2 + (ay_2 - ay_1)^2] \right\} dx_1 dy_1 \\ &= \iint A(ax_1, ay_1) \\ &\cdot \exp \left\{ \frac{i\pi}{\lambda z} [(x_2 - x_1)^2 + (y_2 - y_1)^2] \right\} dx_1 dy_1. \end{aligned} \quad (2)$$

Equation (2) indicates that due to the stretching of the sampling pitch of plane *A*, the effective wavefront of plane *B* will be reconstructed at another plane valued $z' = a^2 z$. At the same time, the original source field $B(x_2, y_2)$, has been changed to $B(ax_2, ay_2)$ with a scaling. This principle is further proved by computer simulation results presented in Figs. 1(b)–1(d). The complex field of plane *A* with sampling pitch $dx_1 = 8 \mu\text{m}$ is calculated by the back propagation from an image [Lena, shown in Fig. 1(b)] located at plane *B*. The distance between planes *A* and *B* is set to $z_1 = 100 \text{ mm}$. Figure 1(c) shows the reconstructed image at plane *B* when the sampling pitch of plane *A* changes to $dx_2 = 1.5 \times 8 \mu\text{m} = 12 \mu\text{m}$, exhibiting a failed reconstruction of the original Lena image. The Lena image is now reconstructed clearly at a new plane calculated by $z_2 = 1.5^2 \times 100 \text{ mm} = 225 \text{ mm}$ as shown in Fig. 1(d). The size of the reconstructed Lena image is scaled by a factor of $a = 1.5$. This simulation results suggest that the reconstruction of the light field of an object can be controlled by adjusting the sampling of the hologram plane. Based on this principle, we propose a method for CGH calculation by designing a nonuniform sampled WRP according to the depth of each object point. As a consequence, the diffraction from the object to this WRP can be calculated simply in

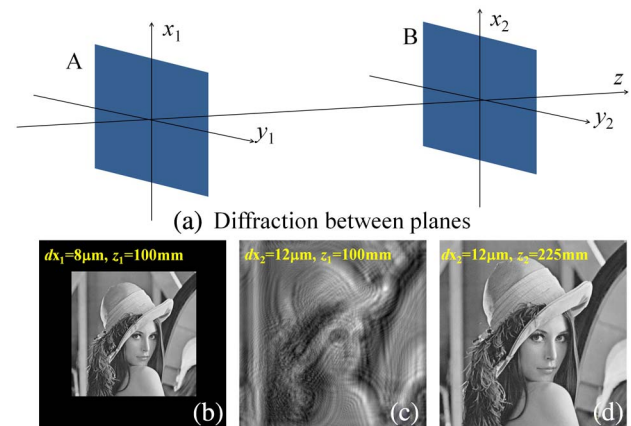


Fig. 1. Diffraction property between two planes.

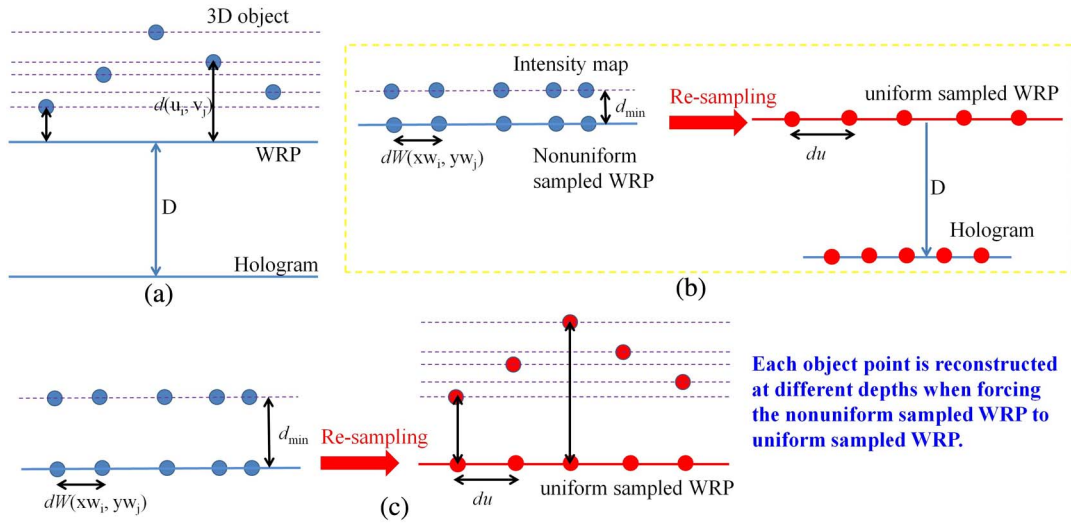


Fig. 2. Principle illustration of our proposed method. (a) Geometry model of the diffraction calculation. (b) Flow diagram of the calculation from 3D object to the hologram. (c) Schematic diagram of 3D object reconstruction from WRP.

only one step by using nonuniform fast Fourier transform (NUFFT)-based algorithm.

B. Calculation of CGH Based on Nonuniform Sampled WRP

The principle of our method is illustrated in Fig. 2. The first step is to design a wavefront recording plane (WRP), which is placed sufficiently close to the object points. Each object point is located at an independent plane as shown in Fig. 2(a), with a transversal pixel pitch du that determines the size of the object. The distance from each point to the WRP is represented by a depth map $d(u_i, v_j)$, where the subscripts i and j denote the index of each point. Then, the intensity of each object points is represented by a 2D intensity map $I(u, v)$ as shown in Fig. 2(b). The created intensity map is located at the plane of distance d_{\min} , where d_{\min} is the minimum value of $d(u_i, v_j)$. The sampling pitch of the intensity map is the same as the WRP, which will be explained below. The nonuniform sampled WRP is designed in this way: for each point in the WRP, its sampling pitch $dW(xw_i, yw_j)$ (also is the sampling pitch of the intensity map) is given according to the depth map:

$$dW(xw_i, yw_j) = \sqrt{d_{\min}/d(u_i, v_j)} \cdot du. \quad (3)$$

Equation (3) reveals the relations between the sampling pitch of WRP and the depth of each object point. In this way, the different depth of each object point gives rise to the nonuniform sampled WRP. Next, the calculation of the nonuniform sampled WRP from the intensity map $I(u, v)$ is accomplished by Fresnel diffraction.

The Fresnel diffraction integral can be expressed in the convolution form derived from Eq. (1):

$$\begin{aligned} W(xw, yw) &= \iint I(u, v) \\ &\quad \cdot \exp \left\{ \frac{i\pi}{\lambda d_{\min}} [(xw - u)^2 + (yw - v)^2] \right\} du dv \\ &= I(u, v) \otimes \exp \left[\frac{i\pi(u^2 + v^2)}{\lambda d_{\min}} \right], \end{aligned} \quad (4)$$

where $W(xw, yw)$ is the light field of the WRP and the sign “ \otimes ” represents the convolution operation. It is well known that the calculation of convolution in Eq. (4) can be written in the form of the Fourier transform as

$$\begin{aligned} W(xw, yw) &= \text{FT}^{-1} \left\{ \text{FT}[I(u, v)] \cdot \text{FT} \left[\exp \left[\frac{i\pi(u^2 + v^2)}{\lambda d_{\min}} \right] \right] \right\} \\ &= \text{FT}^{-1} \{ \text{FT}[I(u, v)] \cdot \text{FT}[b(u, v)] \}, \end{aligned} \quad (5)$$

where FT and FT^{-1} mean the Fourier and inverse Fourier transform. In fact, according to the paraxial approximation analysis [28], the Fourier transform of impulse response function $b(u, v)$ in Eq. (5) can be derived in the form of the angular spectrum method as

$$\begin{aligned} W(xw, yw) &= \text{FT}^{-1} \left\{ \text{FT}[I(u, v)] \right. \\ &\quad \cdot \exp \left(i2\pi d_{\min} \sqrt{\frac{1}{\lambda^2} - f_x^2 - f_y^2} \right) \left. \right\} \\ &= \text{FT}^{-1} \{ \text{FT}[I(u, v)] \cdot T(f_x, f_y) \}, \end{aligned} \quad (6)$$

where f_x and f_y represent the coordinates in the Fourier domain of the planes. Unfortunately, the Fourier transforms in Eq. (6) cannot be calculated by the FFT and inverse FFT operation by virtue of the nonuniform sampled intensity map $I(u, v)$ and the WRP. Therefore, we produce a modified version of the Fresnel diffraction algorithm, in which the nonuniform fast Fourier transform (NUFFT) is employed.

The calculation process of Eq. (6) involves three steps: First, we calculate the uniform sampled angular spectrum from the nonuniform sampled intensity map $I(u, v)$ using type 1 NUFFT. Second, this angular spectrum of the intensity map is multiplied with the transfer function T to obtain the corresponding angular spectrum of the WRP. Finally, the angular spectrum of the WRP is transformed to the nonuniform sampled WRP using the type 2 NUFFT. The whole calculation can be expressed as

$$W(xw, yw) = \text{NUFFT2}\{\text{NUFFT1}[I(u, v)] \cdot T(f_x, f_y)\}. \quad (7)$$

NUFFT1 and NUFFT2 in Eq. (7) denote the first and second type of NUFFT, respectively. After that the calculated nonuniform sampled WRP $W(xw, yw)$ is resampled to a uniform sampled WRP $W(xw', yw')$ by forcing the sampling pitch of all points to du (from $dW(xw_i, yw_j)$ to du) as shown in Fig. 2(b).

Here, we will explain how this resampled WRP can reconstruct each object point at its original depth position. We notice that for each point of the resampled WRP, the sampling pitch is changed from $dW(xw_i, yw_j)$ to du with a scale of $du/dW(xw_i, yw_j)$. Assuming that the depth map has k values totally from d_1, d_2, \dots to d_k , the sampling pitch $dW(xw_i, yw_j)$ also has k values from dW_1, dW_2, \dots, dW_k . In this way, the resampled WRP can be regarded as the sum of k subWRPs, each subWRP contains the points with the same sampling pitch dW_p and the same scale of du/dW_p where subscript p denotes the p th subWRP. The reconstruction from the resampled WRP can be interpreted as the summation of individual reconstruction behavior of each subWRP. According to the principle described in Section 2.A, the reconstruction of object points corresponded to one individual sub-WRP can be expressed as [actually the reconstruction is the inversion of Eq. (4)]

$$I_p(u, v) = \iint W_p(xw, yw) \cdot \exp\left\{\frac{i\pi}{\lambda a_p^2 d_{\min}}[(a_p u - a_p xw)^2 + (a_p v - a_p yw)^2]\right\} dxw dyw, \quad (8)$$

where $W_p(xw, yw)$ is the light field of the p th subWRP, I_p is the intensity of object points at a distance of d_p , $a_p = du/dW_p$ is the scale factor of the pixel pitch in p th subWRP. According to Eq. (8), the object points with intensity I_p will be reconstructed to a new position of d_p with $d_p = (du/dW_p)^2 \times d_{\min}$, which should be their original position according to Eq. (3). Hence, the 3D object $O(u, v, d)$ can be rebuilt by gathering the correct reconstruction of object points with intensity I_p at the desired plane as

$$O(u, v, d) = \sum_{p=1}^k I_p(u, v). \quad (9)$$

It is emphasized that the size of the reconstructed object also has a scale effect owing to the corresponded varying of the pixel pitches of the object from $dW(xw_i, yw_j)$ to du . This is the reason that we need to sample the 2D intensity map $I(u_i, v_j)$ in the same way as the nonuniform sampled WRP at the beginning to compensate for the scaling effect that occurred in the reconstruction, ensuring the 3D object was reconstructed in its original size. Figure 2(c) shows the illustration of the reconstruction from the resampled WRP. By resampling the WRP to a uniform one, each object point is relocated to a new position (original position). The 3D object composed of these point can be reconstructed from the resampled WRP.

In the final step of our method, the diffraction from the re-sampled WRP $W(xw', yw')$ to the hologram $H(x, y)$ is

calculated [see Fig. 2(b)]. This can be accomplished by using the FFT-based Fresnel diffraction algorithm owing to the uniform sampling pitch of the resampled WRP and the hologram. Here we employ *ARSS-Fresnel diffraction* algorithm [6] to calculate the hologram. The remarkable advantage of the ARSS-Fresnel diffraction algorithm is the implementation of diffraction to calculate with different sampling pitches on source and destination planes. Suppose the sampling pitch of the hologram is dx . The parameter s is defining as the ratio of du/dx . The calculation of the final hologram $H(x, y)$ is given by

$$\begin{aligned} H(x, y) &= \iint W(xw, yw) \cdot \exp\left\{\frac{i\pi}{\lambda D}[(x - s \cdot xw)^2 + (y - s \cdot yw)^2]\right\} dxw dyw \\ &= \text{FFT}^{-1}\{\text{FFT}[W(xw, yw) \cdot \exp(i\varphi_1)] \\ &\quad \cdot \text{FFT}[\exp(i\varphi_2) \cdot \text{Rect}]\}, \end{aligned} \quad (10)$$

where Rect is a rectangular function that reduces aliasing noise, φ_1 and φ_2 are quadratic phase term whose detailed expression can be found in [6].

Based on the above description, the computation procedure to generate the CGH of a 3D object can be summarized as below:

- (1). The 2D intensity map and depth map is generated from the 3D object. The wavefront recording plane (WRP) is established.
- (2). Both the intensity map and the WRP are nonuniformly sampled according to the depth map.
- (3). The nonuniform sampled WRP is calculated from the intensity map using Eq. (7).
- (4). The calculated WRP is resampled by forcing its sampling pitches to a uniform value.
- (5). The CGH is obtained by diffraction calculation from the re-sampled WRP using Eq. (10).

In our method, the calculation from 3D voxel information is converted to the calculation between 2D planes, by taking advantage of the idea of variable sampling pitches in the WRP. The calculated CGH can reconstruct the object points at their original depth positions by means of the resampling behavior of the nonuniform sampled WRP. Here, it needs to be stressed that thanks to the extreme close distance from the WRP to the object, the diffraction area from each object point to the WRP is small. A hypothesis can be established that each object point is only affecting a small neighboring region on the WRP. If the sampling pitch in this small region of WRP is changed, only the corresponding object points are relocated to their original depth without effect from other object points, which is very critical to guarantee the success of our method.

Comparing with existing methods for CGH calculation of 3D object, the main and important contribution of our approach reflects in two aspects: on one hand, compared with traditional WRP method, our method calculates the CGH from a 2D image by using NUFFT instead of a point-based method. The calculation in our method is run merely between the planes, providing the ability to accelerate the calculation process by using NUFFT operations. On the other hand,

compared with layer-based methods which use FFT, our method does not need to perform FFT for every depth layer. The calculation time in our method will be invariant as long as the pixel numbers of the intensity map is fixed. In addition, by employing the ARSS–Fresnel diffraction algorithm, the projection of a 3D object with variable sizes is achieved by freely setting the desired sampling pitch during the calculation, which is the key to attain zoomable holographic 3D projection in lensless system.

3. EXPERIMENTAL RESULTS

A. Numerical Simulation Experiments

We first carry out a computer simulation experiment to validate our method. Figure 3 shows a pair of 3D object models used in our experiment. Each model is represented by the intensity image and the depth map as shown in Figs. 3(a)–3(d). The first model is a polygon with regular gradual depth map from the front face to the back, whereas the second model is a car with a depth map generated by 3DMAX. The depth range of both models takes values in the domain $[0.02, 0.04]$ m under the original object size. Note that in our method the depth of each point is defined by its distance to the WRP, not to the hologram.

Figure 3(e) shows the parameters in the calculation of CGH from the 3D model. The intensity image, the WRP, and the hologram are all composed of 1024×1024 pixels. The wavelength of the optical beam, pixel size dx of the hologram, and the distance between the WRP and hologram are set to 532 nm, 8 μ m, and 0.48 m, respectively. For each model, the complex CGH is calculated based on our method with

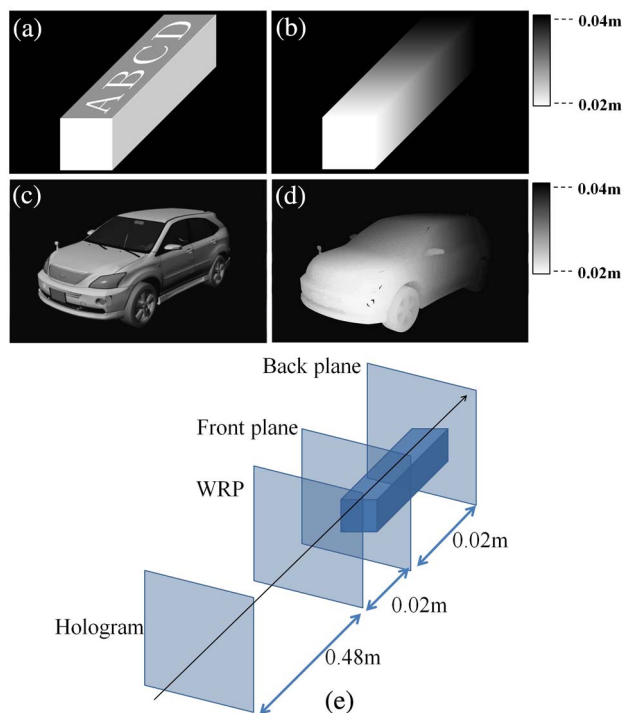


Fig. 3. (a) Intensity map of model *polygon*; (b) depth map of model *polygon*; (c) intensity map of model *car*; (d) depth map of model *car*; (e) geometry model of the calculation of CGH from the 3D model.

the sampling pitch of the intensity map to be 12 μ m (in other words, the object is 1.5 times the hologram size). All the calculation programming in simulation is running on the platform of *Matlab* R2010a. Afterward, the complex CGH is reconstructed numerically by the inverse Fresnel diffraction at two selected focused planes positioned at 0.5 m (the front of the object) and 0.52 m (the back of the object) from the hologram. The results are shown in Figs. 4(a)–4(d), we observe that when the focused plane is at 0.5 m, the front part of the polygon in Fig. 4(a) (closer to the hologram) are clearer than the rest. The clear content moves to the back in Fig. 4(b), when the focused distance is changed to 0.52 m. Similar results are attained for reconstruction of the car model. The above observations will become even more apparent when the details are amplified.

Applying the resampling operation in CGH calculation is a key factor to ensure a correct depth cue of the 3D object, because reconstruction of each object point at different depths is a result due to the resampling from nonuniform pixels to uniform pixels in WRP. For better understanding of this essential point, we conduct an extra simulation experiment in which the CGH is calculated without applying the re-sampling operation to the WRP. The numerical reconstruction at the plane of 0.5 m and 0.52 m from this CGH is presented in Figs. 4(e)

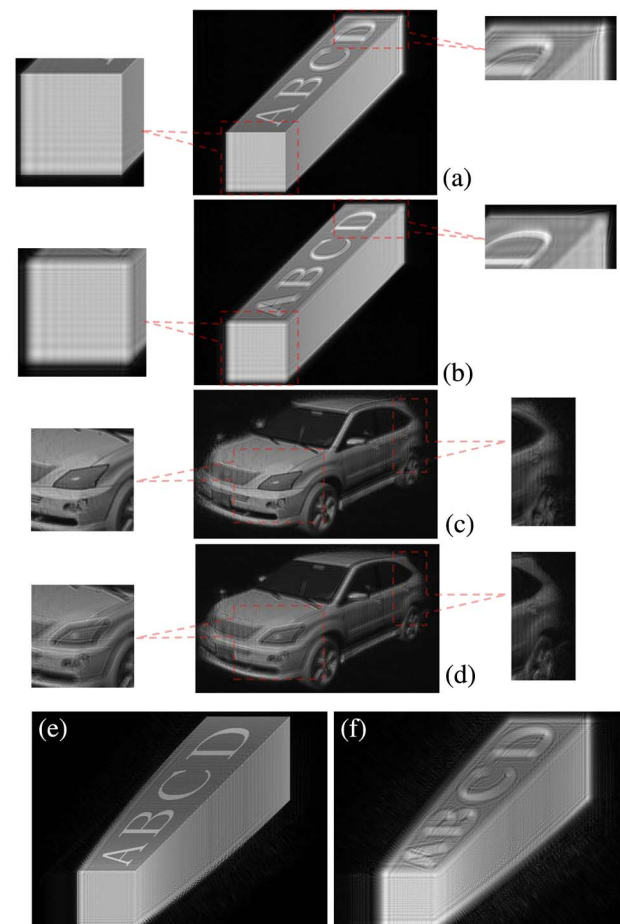


Fig. 4. (a)–(d) are the numerical reconstructions at two focused planes from the complex CGH calculated by our method; (e) and (f) are the numerical reconstructions from the complex CGH calculated without applying re-sampling operation to the WRP.

and 4(f). All the object contents seem to be focused at the front plane and defocused at the back plane. No depth cue effect can be observed compared with the results shown in Figs. 4(a) and 4(b). Distortion also occurred in the reconstructions owing to the fact that by discarding the resampling operation there is no compensation to the scale effect of the object. This simulation reveals the significance of the resampling procedure in the CGH calculation by our method.

A second demonstration is carried out to further prove the ability of projecting a 3D object with zoomable function from the CGH. At present, the pixel pitch of the intensity map of each 3D object is increased to 16 and 20 μm , respectively, which is 2 and 2.5 times the CGH size. For the sake of keeping consistence with the optical experiment in which a phase-only spatial light modulator (SLM) is employed, in the calculation of CGH, an initial random phase is assigned to the intensity map and a phase-only CGH is generated by extracting only the phase term from the calculated complex CGH. Unfortunately, the imposed initial random phase will inevitably cause serious speckle noise in the reconstruction. Therefore, we use the multiple random phase method for further suppressing the speckle noise [7]. Specifically, N different initial random phase distributions are imposed to calculate N different phase-only CGHs by our method. By means of calculating the average intensity from all the reconstructions of N CGHs, we get the speckle-reduced reconstruction. This operation is equivalent to merely observing the reconstructed object when displaying these N different CGHs at a very high rate optically.

Figure 5 shows the reconstructed results from the phase-only CGHs, by using different initial random phase distributions of $N = 20$. Figures 5(a) and 5(c) are the reconstructed results at the plane of 0.5 m in which the front parts of the objects are clearly focused. On the other hand, Figs. 5(b) and 5(d) are the results at 0.52 m with the back of the objects clearly reconstructed. We can observe zoomable projected results in different rows of each figure. The labeled numbers in each image are the pixel pitch of each object model. It is noted that mild speckle noise can still be found in the reconstructions, although the multiple random phase method is adopted. Yet, the quality of the reconstructions can be further improved by increasing the numbers of N , or by combination with iterative-based algorithms (such as classical GS algorithm) to generate the phase-only CGHs, which will be our next work.

B. Optical Experiments

The optical experiment of lensless holographic projection is presented to show the validation of our method. Figure 6 shows the optical system of our lensless zoomable holographic projection which only consists of a laser source with spherical wave illumination and a phase-only SLM (Holoeye Pluto, 1920 \times 1080 pixels with a pixel pitch of 8 μm). The high divergent illumination of the SLM spreads the nondiffracted (or zero-order) light on an area larger than the useful projected 3D object, leading to a far less noticeable visibility. Figure 7 shows the optical reconstructed results of projected 3D objects from the phase-only CGHs calculated by our method. The resultant phase-only CGHs are then multiplied with phase factors of positive lens to cancel the divergence of the illuminating wavefront. The multiple random phase method is used to weaken

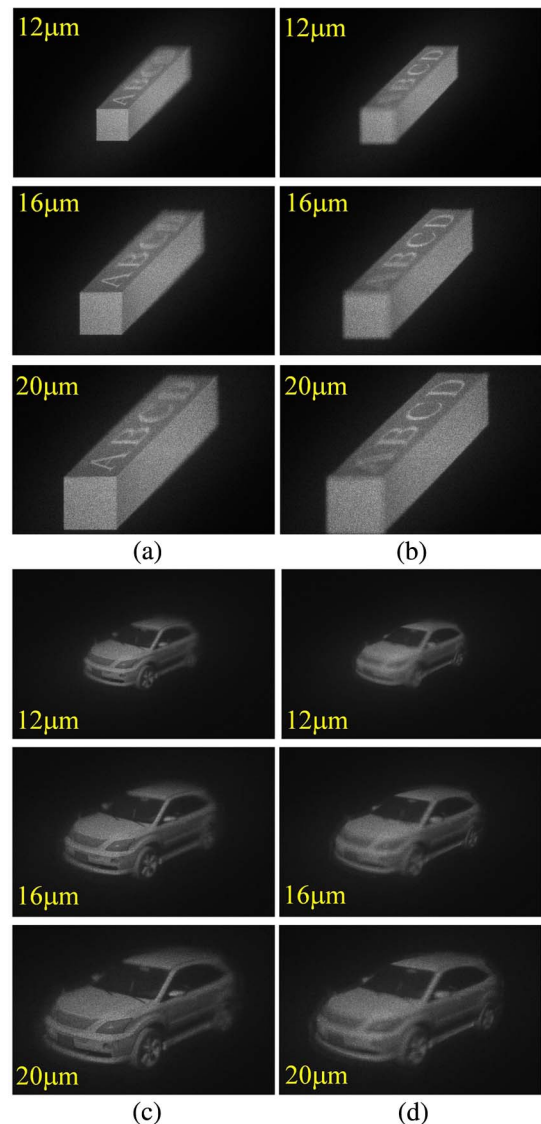


Fig. 5. Numerical reconstructed results at two focused planes from the phase-only CGH calculated by our method. The zoomable effect of each object can be observed.

speckle noise by sequentially loading 20 phase-only CGHs at 60 Hz rate. The reconstructed results are captured directly by the CMOS of the camera at the plane of 0.5 and 0.52 m. It is observed from Figs. 7(a)–7(d) that the results in each optical reconstruction are in agreement with the simulation results presented in Fig. 5, proving that the CGH calculated by

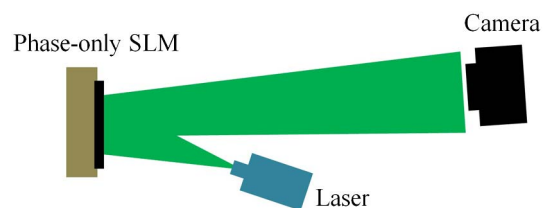


Fig. 6. Optical setup for lensless zoomable holographic projection.

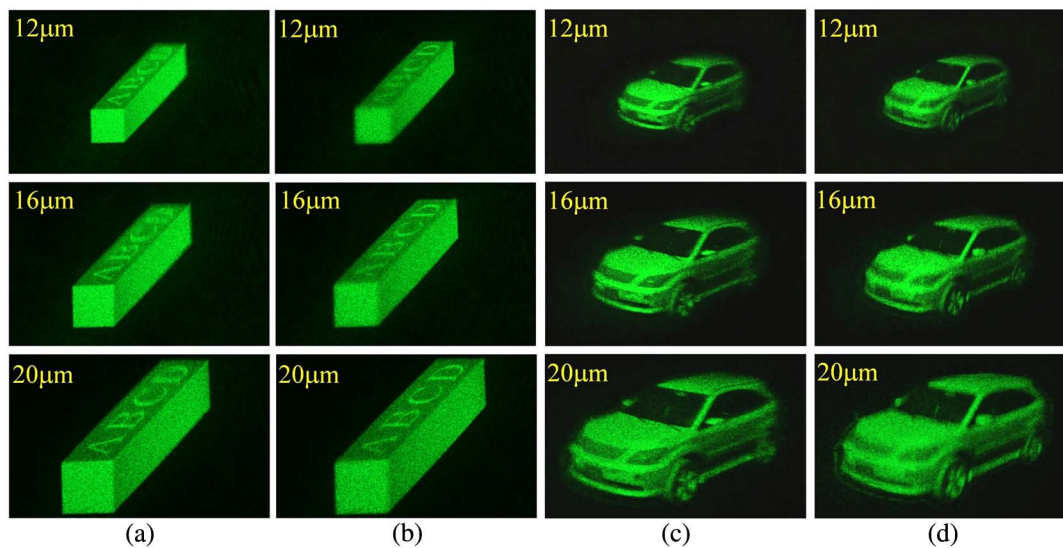


Fig. 7. Optical reconstructed results of projected 3D objects with depth of field from the phase-only CGHs calculated by our method: (a) and (c) focus on the front plane; (b) and (d) focus on the back plane. The zoomable effect of each object can be observed.

our method can project zoomable 3D objects in a lensless holographic projection system.

C. Accommodation Depth Cue

The CGH calculated by our method can reconstruct 3D objects with continuous accommodation depth cue. This feature is further verified by video shooting on the reconstructed object. In the light of the fact that the reconstruction from single static phase-only CGH exists serious speckle noise that prevents the distinction of clear depth cue, so the amplitude type CGH is employed in this experiment. We use the phase-only SLM as amplitude modulator to display the amplitude of CGH. Different from the optical setup shown in Fig. 6, an additional linear polarizer is placed closely in front of the SLM to control the intensity of the reflective light of each SLM pixel. The principle of employing phase-only SLM as an amplitude modulator is found in [29]. In the calculation of CGH, a blazed grating is necessary to separate the desired reconstruction from the zero and conjugated light. Figure 8 shows the numerical and optical reconstructions at different focus planes by displaying the amplitude CGH. Moreover, Visualization 1 and Visualization 2 exhibit the continuous accommodation depth cue in the reconstruction. Visualization 1 shows the dynamic numerical reconstruction from the front to the back of the object, whereas in Visualization 2 the camera is moved between the front and the back plane to capture the continuous depth cue. Here, the observable defect in the optical reconstruction arises from the inaccurate amplitude modulation by the phase-only SLM. The quality of reconstruction could be improved by making use of an amplitude type SLM in the experiment.

4. DISCUSSION

A. Calculation Time

The computation time of our method is evaluated. The computation of Eqs. (7) and (10) can be executed with two NUFFT

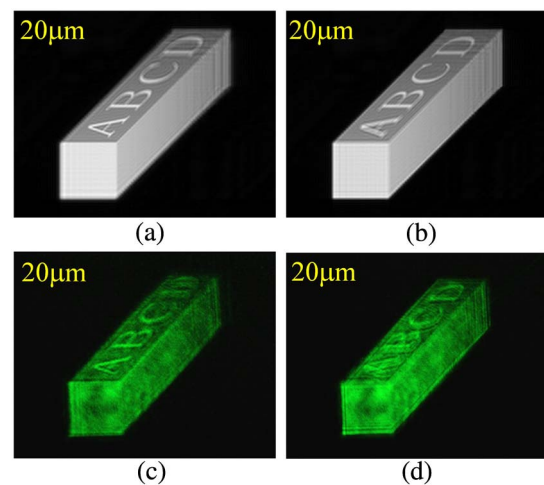


Fig. 8. Numerical reconstructions from amplitude CGH at: (a) front focused plane and (b) back focused plane (Visualization 1). Optical reconstructions from amplitude CGH at: (c) front focused plane and (d) back focused plane (Visualization 2). Visualization 1 and Visualization 2 show the continuous accommodation depth cue in numerical and optical experiments, respectively.

and two FFT operations, while there is an extra time involved for other operations such as transferring the image data and deduction of the sampling pitches. The resampling process of the WRP is basically a computation-free operation in practice. The calculation time of the CGH by our method on an Intel Core i5-5200 (2.20 GHz) CPU is plotted in Fig. 9. Here, the x axis denotes the number of pixels of the 2D intensity map in one dimension. The calculation time is increased by 30 s when the map resolution is increased from 500×500 to 1500×1500 .

Table 1 shows the comparison of calculation time of the CGH using our method and the WRP method reported

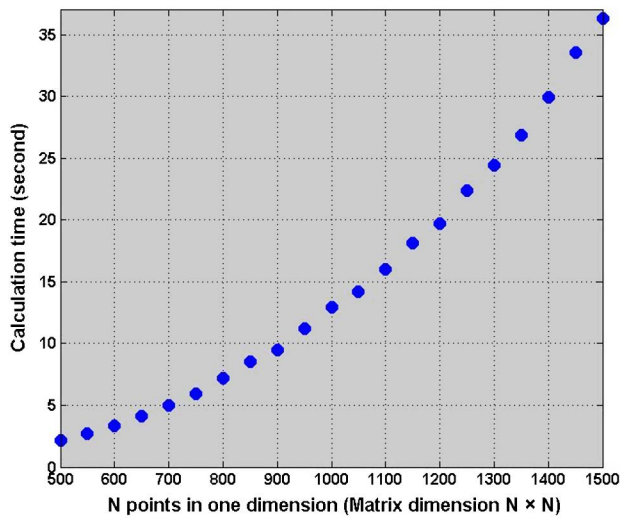


Fig. 9. Calculation time of the CGH by our method.

in [19]. The 2D intensity and depth maps of a 3D object model in CGH calculation is the same with that in Figs. 3(a) and 3(b), while altering the pixel numbers of the intensity map and depth map from 256×256 to 1024×1024 . As shown in the table, by adopting our method using nonuniform sampled WRP, the total calculation time of the CGH of 3D object is far more less than that of the method in [19], showing that our method can greatly improve the computation speed compared with the WRP method.

Table 2 shows the comparison of calculation time of the CGH between our method and the layer-based method. The pixel numbers of the images are 1024×1024 . In the layer-based method, different layer numbers from 50 to 200 are selected. The distance from each layer to the CGH is calculated by fractioning the depth of the 3D object with layer numbers. The image at each layer is obtained according to the depth map. The diffraction from each layer to the CGH is calculated using an angular spectrum method in which two FFTs are adopted. From Table 2, the calculation time by using a layer-based method is increasing proportionally with the number of layers, whereas by our method the calculation time is independent of the numbers of layers.

B. Size of 3D Object

Another feature of our method is the ability to reconstruct a 3D object with variable sizes. This is even attractive because our holographic projection system is lensless. This so-called zoomable function in lensless system is attributed to the employment of a ARSS-Fresnel diffraction algorithm. In this algorithm

Table 1. CGH Calculation Time Comparison with WRP Method

Pixel Numbers	WRP Method (s)	Our Method (s)
256×256	11.9156	0.4353
512×512	24.0182	2.2466
768×768	35.0726	6.3099
1024×1024	47.5324	13.3030

Table 2. CGH Calculation Time Comparison with Layer-Based Method

Number of Layers	Layer-Based Method (s)	Our Method (s)
50	18.2313	13.3030
100	35.7423	13.3030
150	54.1806	13.3030
200	72.4261	13.3030

we can preset pixel pitch at the hologram plane and WRP, respectively, therefore the object with adjustable transversal pixel pitch can be calculated and reconstructed. The overall transversal size of the object can be measured by multiplication of pixel pitch and pixel numbers for each single dimension direction (such as x direction or y direction). However, a maximum value that the object size can reach is determined by the Nyquist limit $L_{\max} = \lambda z / dx$, where dx is the pixel pitch of hologram (also is the pixel pitch of SLM), and z is the distance between the hologram and the object's front plane. Consequently, the maximum transversal pixel pitch of the object should be restricted to $du_{\max} = \lambda z / (N dx)$ once the pixel number N is given. For the situation of our experiment in Section 3, the maximum transverse size that the object can achieve is $L_{\max} = 532 \text{ nm} \times 0.5 \text{ m} / 8 \mu\text{m} = 0.03325 \text{ m}$ which is four times or so larger than the size of the hologram ($8 \mu\text{m} \times 1024 = 0.0082 \text{ m}$). Figure 10 presents the numerical reconstructions (at 0.5 m) of CGHs calculated from the object with pixel pitch rising from $12 \mu\text{m}$ to the maximum value ($0.03325 \text{ m} / 1024 \approx 32 \mu\text{m}$), proving the capability of our method to reconstruct a 3D object to its maximum limit with zoomable function in lensless holographic projection system.

C. NUFFT Algorithm

The NUFFT algorithm code involved in our method is created by Greengard and Lee [23]. The calculation speed is affected by the oversampling ratio that is defined by the ratio of the oversampling pixel numbers and the numbers of target image pixels. The chosen oversampling ratio lies on the desired precision which acts as an input parameter in the algorithm code. In our experiment, we use 12 bits of accuracy, and the oversampling rate is 2 accordingly. It is emphasized that once the oversampling ratio is chosen, the oversampling number is only determined by the pixel numbers of the depth map that is independent of depth layers. For example, in our experiment, the matrix in the calculation is 1024×1024 , with used precision condition the oversampling number is $1024 \times 2 = 2048$ in one

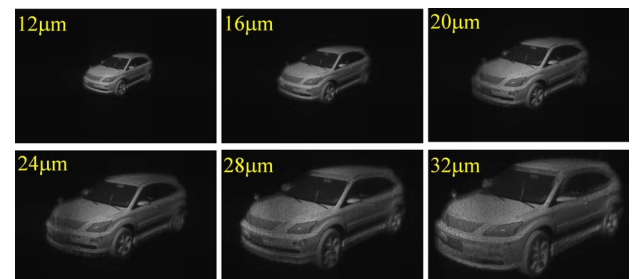


Fig. 10. Numerical reconstructions of a 3D object with different sizes.

dimension. No matter how many layers there are, the oversampling number will be fixed as long as the matrix dimension is preset.

The calculation error in the NUFFT algorithm may cause the error in CGH calculation and reconstruction. Since 12 bits of accuracy are used in the calculation of NUFFT, the error of NUFFT algorithm is very small. However, one drawback of our method is that the depth map of the 3D object should be required to be smooth enough. Any sharp change between adjacent points in depth may render an error of depth in reconstruction. This is because two adjacent object points with large disparity in depth will cause entire overlapping of diffraction region at the WRP plane, under which our method becomes invalid. This problem still remains to be solved for our future effort.

5. CONCLUSION

In this investigation, a method for simple calculation of the CGH from a 3D object has been proposed. The CGH is generated by diffraction calculation from a 2D planar image instead of 3D object voxels, in which only two NUFFT and two FFT operations are involved, giving rise to great reduction of the data amount in the calculation process. The experimental results exhibit that the generated CGH is able to project zoomable 3D objects with clear depth information. Literally, we believe that our proposed method shows potential in the application of lensless holographic projection and display.

Funding. 973 Program (2013CB328803); 863 Program (2013AA013904, 2015AA016301); National Natural Science Foundation of China (NSFC) (61377003, 61306140); Natural Science Foundation of Jiangsu Province (BK20130618); Scientific Research Foundation for Advanced Talents, Nanjing Normal University, China (184080H20162, 184080H20178); Jiangsu Province University Important Natural Science Research Project, China (14KJA140001).

REFERENCES

1. E. Buckley, "Holographic projector using one lens," *Opt. Lett.* **35**, 3399–3401 (2010).
2. E. Buckley, "Holographic laser projection," *J. Display Technol.* **7**, 135–140 (2011).
3. M. Makowski, M. Sypek, I. Ducin, A. Fajst, A. Siemion, J. Suszek, and A. Kolodziejczyk, "Experimental evaluation of a full-color compact lensless holographic display," *Opt. Express* **17**, 20840–20846 (2009).
4. M. Makowski, I. Ducin, K. Kakarenko, J. Suszek, M. Sypek, and A. Kolodziejczyk, "Simple holographic projection in color," *Opt. Express* **20**, 25130–25136 (2012).
5. M. Makowski, "Minimized speckle noise in lens-less holographic display by pixel separation," *Opt. Express* **21**, 29205–29216 (2013).
6. T. Shimobaba, T. Kakue, N. Okada, M. Oikawa, Y. Yamaguchi, and T. Ito, "Aliasing-reduced Fresnel diffraction with scale and shift operations," *J. Opt.* **15**, 075405 (2013).
7. T. Shimobaba, M. Makowski, T. Kakue, M. Oikawa, N. Okada, Y. Endo, R. Hirayama, and T. Ito, "Lensless zoomable holographic projection using scaled Fresnel diffraction," *Opt. Express* **21**, 25285–25290 (2013).
8. M. Lucente, "Interactive computation of holograms using a look-up table," *J. Electron. Imaging* **2**, 28–34 (1993).
9. S.-C. Kim and E.-S. Kim, "Fast computation of hologram patterns of a 3D object using run-length encoding and novel look-up table methods," *Appl. Opt.* **48**, 1030–1041 (2009).
10. S.-C. Kim and E.-S. Kim, "Effective generation of digital holograms of three-dimensional objects using a novel look-up table method," *Appl. Opt.* **47**, D55–D62 (2008).
11. T. Haist, M. Schonleber, and H. J. Tiziani, "Computer-generated holograms from 3D-objects written on twisted-nematic liquid crystal display," *Opt. Commun.* **140**, 299–308 (1997).
12. H. Zheng, Y. Yu, T. Wang, and L. Dai, "High-quality three-dimensional holographic display with use of multiple fractional Fourier transform," *Chin. Opt. Lett.* **7**, 1151–1154 (2009).
13. J. Xia and H. Yin, "Three-dimensional light modulation using phase-only spatial light modulator," *Opt. Eng.* **48**, 020502 (2009).
14. K. Matsushima and S. Nakahara, "Extremely high-definition full-parallax computer-generated hologram created by the polygon-based method," *Appl. Opt.* **48**, H54–H63 (2009).
15. Y. Z. Liu, J. W. Dong, Y. Y. Pu, B. C. Chen, H. X. He, and H. Z. Wang, "High-speed full analytical holographic computations for true-life scenes," *Opt. Express* **18**, 3345–3351 (2010).
16. Y. Pan, Y. Wang, J. Liu, X. Li, and J. Jia, "Fast polygon-based method for calculating computer-generated holograms in three-dimensional display," *Appl. Opt.* **52**, A290–A299 (2013).
17. T. Shimobaba, N. Masuda, and T. Ito, "Simple and fast calculation algorithm for computer-generated hologram with wavefront recording plane," *Opt. Lett.* **34**, 3133–3135 (2009).
18. T. Shimobaba, H. Nakayama, N. Masuda, and T. Ito, "Rapid calculation algorithm of Fresnel computer-generated hologram using look-up table and wavefront-recording plane methods for three-dimensional display," *Opt. Express* **18**, 19504–19509 (2010).
19. J. Weng, T. Shimobaba, N. Okada, H. Nakayama, M. Oikawa, N. Masuda, and T. Ito, "Generation of real-time large computer generated hologram using wavefront recording method," *Opt. Express* **20**, 4018–4023 (2012).
20. P. W. M. Tsang and T.-C. Poon, "Fast generation of digital holograms based on warping of the wavefront recording plane," *Opt. Express* **23**, 7667–7673 (2015).
21. A. Dutt and V. Rokhlin, "Fast Fourier transforms for nonequispaced data," *SIAM J. Sci. Comput.* **14**, 1368–1393 (1993).
22. Q. H. Liu and N. Nguyen, "An accurate algorithm for nonuniform fast Fourier transforms (NUFFT)," *IEEE Microwave Guided Wave Lett.* **8**, 18–20 (1998).
23. L. Greengard and J. Y. Lee, "Accelerating the nonuniform fast Fourier transform," *SIAM Rev.* **46**, 443–454 (2004).
24. T. Shimobaba, K. Matsushima, T. Kakue, N. Masuda, and T. Ito, "Scaled angular spectrum method," *Opt. Lett.* **37**, 4128–4130 (2012).
25. T. Shimobaba, T. Kakue, M. Oikawa, N. Okada, Y. Endo, R. Hirayama, and T. Ito, "Nonuniform sampled scalar diffraction calculation using nonuniform fast Fourier transform," *Opt. Lett.* **38**, 5130–5133 (2013).
26. C. Chang, J. Xia, J. Wu, W. Lei, Y. Xie, M. Kang, and Q. Zhang, "Scaled diffraction calculation between tilted planes using nonuniform fast Fourier transform," *Opt. Express* **22**, 17331–17340 (2014).
27. C. Chang, J. Xia, and W. Lei, "One step hologram calculation for multi-plane objects based on nonuniform sampling," *Chin. Opt. Lett.* **12**, 060020 (2014).
28. J. W. Goodman, *Introduction to Fourier Optics* (Roberts & Company, 2004).
29. W. Harm, A. Jesacher, G. Thalhammer, S. Bernet, and M. R. Marte, "How to use a phase-only spatial light modulator as a color display," *Opt. Lett.* **40**, 581–584 (2015).